The Astrophysical Journal, 945:21 (6pp), 2023 March 1 https://doi.org/10.3847/1538-4357/acb81d

Advanced γ-Ray Emission Studies of G15.4+0.1 with Fermi-LAT: Evidence of Escaping Cosmic Rays Interacting with Surrounding Molecular Clouds

Yuan Li[1], Yuliang Xin[1], Siming Liu[1], and Yu He[1]
School of Physical Science and Technology, Southwest Jiaotong University, Chengdu 610031, People's Republic of China; ylxin@swjtu.edu.cn (YLX), liusm@swjtu.edu.cn (SML)

Received 2022 November 18; revised 2023 January 12; accepted 2023 January 31; published 2023 March 2

Abstract

We present an analysis of γ-ray emission in the direction of supernova remnant (SNR) G15.4+0.1 with 13 yr Fermi Large Area Telescope data. There are three point-like GeV sources in this region: one is spatially coincident with the TeV source HESS J1818-154 and is interpreted as the counterpart of HESS J1818-154. Its γ-ray spectrum can be well fitted by a single power law with an index of 2.3. The other two sources with log-parabola spectra are spatially coincident with dense regions of surrounding molecular clouds revealed by CO observations. Their γ-ray emission originates from hadronic π^0 decay due to inelastic collisions between nuclei in the clouds and cosmic rays accelerated in and escaping from SNR G15.4+0.1. The total energy of the escaping protons is about 10^{48} erg, assuming a point-like instantaneous injection. However, the inferred diffusion coefficients are lower than the typical Galactic value.

Unified Astronomy Thesaurus concepts: Gamma-ray sources (633); Gamma-ray astronomy (628); Supernova remnants (1667)

1. Introduction

Supernova remnants (SNRs) are widely believed to be the most probable acceleration sites of Galactic cosmic rays (CRs) below PeV energy of the spectral knee (Hillas 2005). These high-energy CRs produce γ-ray emissions through different radiation mechanisms, including inverse Compton scattering and/or the bremsstrahlung process of high-energy electrons (leptonic model) and the decay of neutral pion mesons that are produced in collisions between accelerated protons and the ambient materials (hadronic model). γ-ray emission is expected from dense molecular clouds (MoCs) illuminated by CRs escaping SNRs. Actually, γ-ray emissions from this type of source have been detected by the Fermi Large Area Telescope (Fermi-LAT), including γ-Cygni (MAGIC Collaboration et al. 2023), IC443 (Abdo et al. 2010; Ackermann et al. 2013), W44 (Uchiyama et al. 2012; Peron et al. 2020), W28 (Aharonian et al. 2008; Li & Chen 2010; Hanabata et al. 2014), and W51C (Abdo et al. 2009). The intense GeV γ-ray emissions from these SNRs generally originate from the hadronic process between accelerated protons and nuclei in dense MoCs. Especially, the γ-ray spectra of W51C, W44, and IC443 have shown the spectral feature of π^0 decay, which is considered to be the most direct evidence for the acceleration of relativistic nuclei in SNRs (Giuliani et al. 2011; Ackermann et al. 2013; Jogler & Funk 2016).

Diffusive shock acceleration (DSA) operating at expanding shock waves of SNRs is widely regarded as the mechanism converting the kinetic energy released by supernova explosions into the energy of CRs (Malkov & Drury 2001). According to the DSA mechanism, CRs being accelerated at the shock of SNRs could be scattered by self-generated magnetic turbulence, and the highest-energy CRs in the shock precursor are expected to escape from SNRs due to relatively inefficient scattering. The DSA mechanism generally predicts that a substantial fraction of the shock energy is carried away by escaping CRs. When MoCs surround these SNRs, these clouds could be illuminated by the escaping CRs, producing γ-ray emission through the *pp* interactions. And the γ-ray spectrum depends on the number of nuclear CRs that is released and on the diffusion coefficient in the interstellar medium (ISM; Aharonian & Atoyan 1996; Aharonian et al. 2004; Rodriguez Marrero et al. 2008; Gabici et al. 2009). For γ-ray sources associated with clouds illuminated by escaped CRs from nearby SNRs, the measured γ-ray spectrum can therefore help to study the diffusion process and constrain the energy dependence of the diffusion coefficient in the ISM (Aharonian & Atoyan 1996; Ohira et al. 2011).

G15.4+0.1 was first identified as a faint SNR during the Galactic plane survey by the Very Large Array (VLA) at 330 MHz (Brogan et al. 2006). Subsequent observation of the radio shell was reported with a diameter of nearly 15′ (Castelletti et al. 2013), and the global spectral index is 0.62 ± 0.03 from 330 to 4800 MHz (Supan et al. 2015; Su et al. 2017). In other energy bands, H. E. S. S. Collaboration et al. (2014) detected the point-like TeV γ-ray source HESS J1818-154, which is spatially consistent with the SNR. A molecular gas complex is likely associated with the SNR at a distance of 4.8 kpc (Supan et al. 2015). An age of 8200 yr is obtained with a dynamical evolution model for the SNR (Chevalier 1974).

However, the origin of the γ-ray emission from HESS J1818-154 has not been identified. The data analysis of XMM-Newton revealed an extended X-ray source coincident with the TeV γ-ray emission, implying an energy-dependent morphology (H. E. S. S. Collaboration et al. 2014). Taking into account the morphological consistence between the X-ray and TeV γ-ray emission, H. E. S. S. Collaboration et al. (2014) suggested that HESS J1818-154 may be associated with a pulsar wind nebula (PWN) powered by a hypothetical pulsar placed in the interior of the remnant. In this scenario, the TeV γ-ray emission is produced via inverse Compton scattering of high-energy electrons from a PWN with the interstellar radiation field. Another possible explanation is that the γ-ray emission from HESS J1818-154 is generated by collisions of high-energy protons accelerated by the shock of G15.4+0.1 and the ambient dense materials (Castelletti et al. 2013).

In this work, we report analyses of the GeV γ-ray emission toward SNR G15.4+0.1 using 13 yr Fermi-LAT data in the energy range of 300 MeV–1 TeV in Section 2. The ^{13}CO($J = 1$-0) observations of MoCs in this region are shown in Section 3 to reveal the origin of the γ-ray emission. In Section 4 we discuss interpretations of the GeV γ-ray emission, followed by conclusions in Section 5.

2. Fermi-LAT Data Analysis

Fermi-LAT is sensitive to γ-rays with energies from 20 MeV to over 300 GeV, and it has continuously monitored the sky since 2008 (Atwood et al. 2009). The Pass 8 data with the event class "P8R3_SOURCE" (evclass = 128) from 4 August 2008 to 4 August 2021 are taken to study the GeV emission around SNR G15.4+0.1. And the γ-ray events are selected with the standard data-quality selection criteria (`DATA_QUAL > 0`)&&(`LAT_CONFIG==1`). To minimize the contamination from the Earth limb, the maximum zenith angle is set to be 90°. In this work, the publicly available software Fermitools (ver. 1.2.23) is used to preform the data analysis. Data within a $14^\circ \times 14^\circ$ region of interest (ROI) centered at the position of G15.4+0.1 are considered for the binned maximum likelihood analysis (Mattox et al. 1996), and the instrumental response function "P8R3_SOURCE_V3" is used. The diffuse Galactic interstellar emission (IEM; `gll_iem_v07.fits`), the isotropic emission (`iso_P8R3_SOURCE_V3_v1.txt`), and all sources listed in the incremental version of the fourth Fermi-LAT catalog (4FGL-DR3; Abdollahi et al. 2020, 2022) are included in the background model. And all sources within 5° from the center of ROI are set free, together with the normalizations of IEM and isotropic emission. The maximum likelihood test statistic (TS) is used to estimate the significances of the γ-ray sources, which is defined as $\mathrm{TS} = 2(\ln \mathcal{L}_1 - \ln \mathcal{L}_0)$, where $\mathcal{L}_1$ and $\mathcal{L}_0$ are maximum likelihood values for the background with and without the target source (null hypothesis).

2.1. Spatial Analysis

In the region around G15.4+0.1, two γ-ray sources are listed in the 4FGL-DR3 catalog (4FGL J1818.6-1533 and 4FGL J1819.9-1530), and both are assumed to be point-like without identified counterparts. We first created a $1^\circ\!.0 \times 1^\circ\!.0$ in the TS map with the command *gttsmap* by subtracting the emission from the diffuse backgrounds and all 4FGL-DR3 sources (except 4FGL J1818.6-1533 and 4FGL J1819.9-1530) in the best-fit model using the events in the energy range of 3 GeV–1 TeV, which is shown in the left panel of Figure 1. The TS map shows a strong γ-ray excess around 4FGL J1818.6-1533. In order to determine the best spatial template of the γ-ray emission in this region, we first added a single point-like source (SrcA) to the model (Model 1) and optimized its localization using the *gtfindsrc* command. After subtracting the γ-ray emission from SrcA, there are still two significant excesses, as shown in the middle panel of Figure 1. We therefore additionally added two point-like sources (SrcB and SrcC) to the model (Model 2) and refitted their positions with gtfindsrc. The derived best-fit positions of SrcA/B/C and their 68% error radii above 3 GeV are (R.A. = $274^\circ\!.760$, decl. = $-15^\circ\!.558$, $r_{68} = 0^\circ\!.037$), (R.A. = $274^\circ\!.516$, decl. = $-15^\circ\!.504$, $r_{68} = 0^\circ\!.025$), and (R.A. = $275^\circ\!.109$, decl. = $-15^\circ\!.507$, $r_{68} = 0^\circ\!.030$), respectively. Compared with the single point-source model (Model 1), the scenario with three point sources is significantly improved with $\Delta\mathrm{TS} = 43.8$, which corresponds to a significance level of 5.79σ with four degrees of freedom (dof).

We also attempted to fit this γ-ray emission with a single extended source template, and we tested a single uniform disk (Model 3) and two-dimensional Gaussian template (Model 4). The Fermipy tool (Wood et al. 2017) is used to quantitatively evaluate the extension and location of these two templates. When the maximum likelihood values are compared with the values of Model 2, a single extended source template is not favored. Meanwhile, we also tested the templates of an extended source plus the scenario with two point-like sources. In this case, SrcA is considered as an extended source with a uniform disk (Model 5) or a two-dimensional Gaussian (Model 6) assumption, in which SrcB and SrcC are still considered to be point-like sources in the model. Then we compared the overall maximum likelihood of the extended template ($\mathcal{L}_{\mathrm{ext}}$; alternative hypothesis) with that of the point-like source model ($\mathcal{L}_{pt}$; null hypothesis), and defined the significance of the extended model to be $\mathrm{TS}_{\mathrm{ext}} = 2(\ln \mathcal{L}_{\mathrm{ext}} - \ln \mathcal{L}_{pt})$. The alternative hypothesis is significantly preferred to the null hypothesis only if $\mathrm{TS}_{\mathrm{ext}} > 16$ (Lande et al. 2012), but the value of $\mathrm{TS}_{\mathrm{ext}}$ is calculated to be only 2.2/7.0, which suggests no significant spatial extension for SrcA. The scenario with three point sources (Model 2) is sufficient to describe the γ-ray emission in this region.

In addition, we also used the Akaike information criterion (AIC; Akaike 1974) to compare the difference between these models, which is defined as $\mathrm{AIC} = 2\mathrm{k}—2\ln \mathcal{L}$. The minimum AIC values is preferred. Here k is the number of the degrees of freedom, and $\mathcal{L}$ is the likelihood value of the corresponding model. The calculated values of δ AIC compared with Model 1 are listed in Table 1. They also suggest that the extended source scenrios have no significant imporvements. We therefore adopted the template with three point sources (Model 2) for the further analysis.

By dividing the energy range of 300 MeV–1 TeV into nine logarithmically euqal bins and performing the same likelihood fitting analysis for each energy bin, we obtained the spectral energy distribution (SED) of SrcB. It is shown as the cyan dots in the middle panel of Figure 2. To test whether the upturn in the SrcB spectrum is intrinsic or is due to two overlapping sources, we also performed the same likelihood fitting using events with a low energy from 300 MeV to 3 GeV, and only photons with an event class of PSF3 (evtype = 32) were adopted. After subtracting the contributions from SrcA and SrcC, the γ-ray emission around SrcB with photons between 300 MeV and 3 GeV is shown in the right panel of Figure 1. The relocalization of SrcB with *gtfindsrc* gives the coordinate (R.A. = $274^\circ\!.440$, decl. = $-15^\circ\!.382$) with a 68% error radius of $r_{68} = 0^\circ\!.070$ in the low-energy range, which is different from that in the high-energy range of 3 GeV–1 TeV. Thus we suggest that SrcB probably consists of two different sources in the full energy range of 300 MeV–1 TeV. These sources are labeled SrcB1 for the 300 MeV–3 GeV source and SrcB2 for the 3 GeV–1 TeV source.

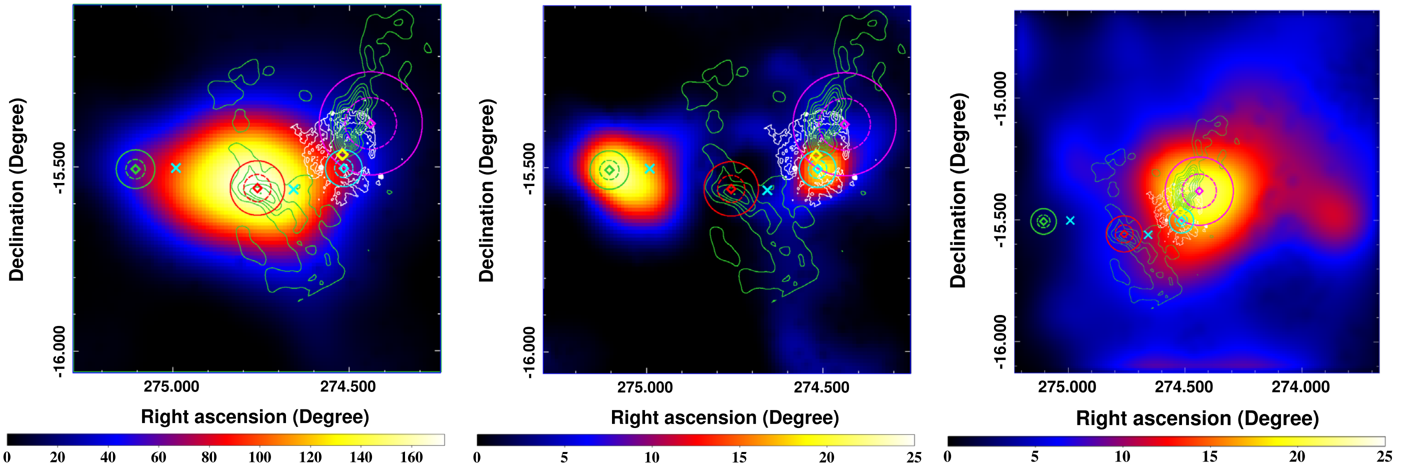

Figure 1. Left: $1\overset{\circ}{.}0 \times 1\overset{\circ}{.}0$ TS map centered at SrcA by subtracting the diffuse background and 4FGL-DR3 sources (except for 4FGL J1818.6-1533 and 4FGL J1819.9-1530, which are indicated by two cyan crosses) using the events in the energy range of 3 GeV–1 TeV. The red, magenta, cyan, and green diamonds represent the positions of SrcA, SrcB1, SrcB2, and SrcC, respectively. And the corresponding 68% and 95% error radii are shown as the dashed and solid circles. The position of the TeV source HESS J1818-154 is marked by the yellow diamond (H. E. S. S. Collaboration et al. 2018). The white contours show the radio image of SNR G15.4 +0.1 at 3.3 GHz from the VLA (Brogan et al. 2006). And the green contours represent the ^{13}CO(J = 1-0) intensity integrated over a velocity range between 46.0 and 50.3 km s^{-1} in this region. Middle: Same as the left panel after subtracting SrcA. Right: $1\overset{\circ}{.}5 \times 1\overset{\circ}{.}5$ TS map centered at SrcB1 after subtracting the contribution from SrcA/C using events with a PSF3 type from 300 MeV to 3 GeV.

Table 1
Spatial Models Tested for the GeV γ-Ray Emission above 3 GeV

Spatial Model	−log(Likelihood)	dof[a]	ΔAIC[b]
Model 1(1point)	−21793	0	0
Model 2 (3point)	−21815	4	−36
Model 3 (Disk)	−21805	3	−18
Model 4 (Gaussian)	−21807	3	−22
Model 5 (Disk+2point)	−21816	5	−36
Model 6 (Gaussian+2point)	−21818	5	−40

Notes.
[a] Additional dofs compared to Model 1.
[b] Calculated with respect to Model 1.

Table 2
Results of the Spectral Analysis in the Energy Range of 300 MeV–1 TeV

SrcA	SrcB1	SrcB2	DoF	−log(Likelihood)	ΔTS[a]
PL	PL	PL	6	−9844757	0
LogPb	PL	PL	7	−9844805	96
LogPb	PL	LogPb	8	−9844809	104
LogPb	LogPb	PL	8	−9844819	124
LogPb	LogPb	LogPb	9	−9844811	108

Note.
[a] Calculated with respect to the power-law case.

By adopting the spatial model including SrcA, B1, B2, and C and assuming their spectra to be power laws, we also performed the separate likelihood fittings in the low- and high-energy ranges. The fitting results in the 300 MeV–3 GeV energy band show that the emission around SrcB is dominated by SrcB1 with a soft spectral index of 2.71 ± 0.31, and the TS value of SrcB2 is only 1.5. In the energy range of 3 GeV–1 TeV, however, the TS value of SrcB1 is lower than 1.0, and SrcB2 has a significant γ-ray emission with a harder sperctral index of 2.44 ± 0.30.

2.2. Spectral Analysis

With the best-fit spatial model including SrcA/B1/B2/C in this region, the spectral analysis is derived with a power law ($dN/dE \propto E^{-\alpha}$) or/and log-parabola (LogPb; $dN/dE \propto E^{-(\alpha+\beta\log(E/E_b))}$) model for SrcA/B1/B2 using the data from 300 MeV to 1 TeV. For SrcC, there is no potential counterpart that can produce γ-ray emission within its 95% error circle through the SIMBAD[1] database. SrcC is therefore regarded to be a background point source, and its spectrum is fixed to be a power-law model. By fixing the spectra of SrcB1 and SrcB2 to be power-law models, we first tested the spectral curvature of SrcA with power-law and LogPb models. The fitting results listed in Table 2 show a significant curvature for SrcA with $\mathrm{TS_{curve}} = 2(\ln \mathcal{L}_{\mathrm{LogPb}}\text{-}\ln \mathcal{L}_{\mathrm{PL}}) = 95.7$, which corresponds to a significance level of 9.78σ with one additional dof (Abdollahi et al. 2020). By adopting the LogPb model for SrcA, we then made a comparison between multiple spectral shapes for SrcB1 and SrcB2. The spectrum of SrcB1 is well described by a log-parabola with $\alpha = 2.99 \pm 0.54$ and a significant curvature ($\mathrm{TS_{curve}} = 28.5$, or an improvement of 5.34σ with respect to a power-law model) of $\beta = 3.72 \pm 1.05$. The integrated photon flux of SrcB1 from 300 MeV to 1 TeV is calculated to be $(9.08 \pm 2.24) \times 10^{-9}$ ph cm^{-2} s^{-1}. The spectrum of SrcB2 can be well described by a power-law model with an index of 2.30 ± 0.15 and an integrated photon flux between 300 MeV and 1 TeV of $(4.63 \pm 1.78) \times 10^{-9}$ ph cm^{-2} s^{-1}, as shown in Table 3.

In order to obtain the SEDs of SrcA/B1/B2, the data in the 300 MeV–1 TeV energy range were binned into nine logarithmically equal intervals, and the same likelihood fitting analysis was performed for each interval. The flux normalizations of all sources are left free, but the spectral indices are fixed. For the interval with a TS value of SrcA, B1, and B2 lower than 5.0, the upper limit is calculated with a 95% confidence level using the Bayesian method (Helene 1983). The resulting SEDs are shown in Figure 2, together with the global best-fit spectra in the energy range of 300 MeV–1 TeV.

---

[1] http://simbad.u-strasbg.fr/simbad/sim-fbasic

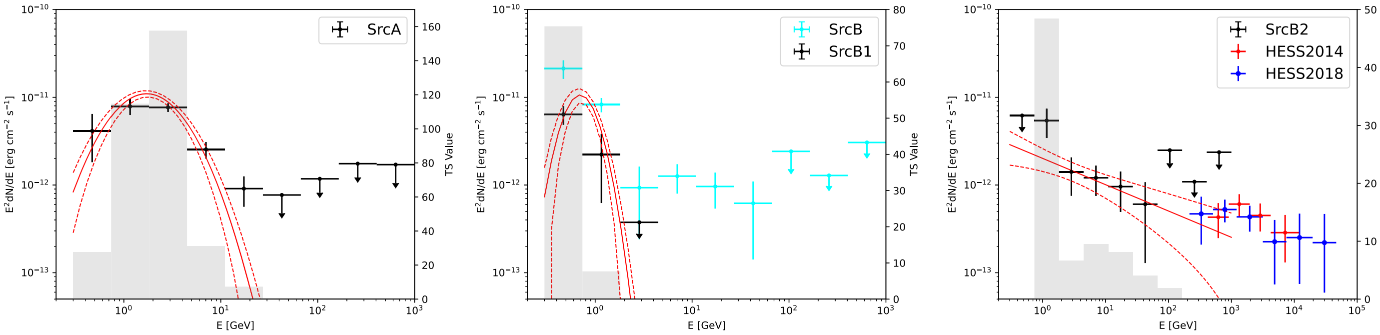

Figure 2. SEDs of SrcA (left), SrcB1 (middle), and SrcB2 (right). The black dots show the results of Fermi-LAT data, with arrows indicating the 95% upper limits. The gray histogram denotes the TS value for each energy interval. The solid and dashed red lines are the global best-fit spectra and their 1σ statistic error in the energy range of 300 MeV–1 TeV. The cyan dots in the middle panel show the SED of SrcB using the coordinate derives from the analysis between 3 GeV and 1 TeV. The red and blue data points in the right panel show the HESS observations from H. E. S. S. Collaboration et al. (2014) and H. E. S. S. Collaboration et al. (2018), respectively.

Table 3
Parameters of the Best-fit Spectral Models in the Energy Range of 300 MeV–1 TeV

Source	Index/α	β	TS Value	Photon Flux (ph cm^{-2} s^{-1})
SrcA	2.26 ± 0.14	0.85 ± 0.17	410	$(9.7 \pm 1.8) \times 10^{-9}$
SrcB1	2.99 ± 0.54	3.72 ± 1.05	100	$(9.1 \pm 2.2) \times 10^{-9}$
SrcB2	2.30 ± 0.15	⋯	40	$(4.6 \pm 1.8) \times 10^{-9}$

The SED of SrcB2 shows that the Fermi-LAT data smoothly connect with the TeV spectrum of HESS J1818-154. Considering the spatial coincidence between SrcB2 and HESS J1818-154 shown in Figure 1, we suggest that SrcB2 is the GeV counterpart of HESS J1818-154.

3. CO Observations

To reveal the γ-ray origin of SrcA, B1, and B2, we make use of the CO data from the Boston University-Five College Radio Astronomy Observatory (BU-FCRAO) Galactic Ring Survey (GRS) to search for the MoCs around the region of SNR G15.4+0.1 (Jackson et al. 2006). The GRS data offer excellent sensitivity (<0.4 K) and a higher spectral resolution (0.2 km s^{-1}), angular resolution (46″), and sampling (22″). We inspect the ^{13}CO($J = 1$-0) line profiles of the MoCs toward G15.4+0.1, to search for kinematic evidence for the gas distribution due to external interaction (Frail & Mitchell 1998; Reach et al. 2005; Kilpatrick et al. 2016). The velocity distribution of the CO content shows a clear excess in the velocity range of 46.0–50.3 km s^{-1} (Castelletti et al. 2013), which is also spatially consistent with the intensity of the γ-ray emission in this region. As shown in Figure 3, SrcA coincides well with a dense region of the gas distribution far from G15.4+0.1 (called clump A), and SrcB1 coincides well with the densest region (called clump B), which coincides with the radio shell of G15.4+0.1.

To calculate the column density of H_2 in the two clumps, N_{H_2}, meaning $N_{H_2} = X_{CO} \times W_{CO}$, we adopted a conversion factor of $X_{CO} = 2 \times 10^{20}$ cm^{-2} (K km s^{-1})$^{-1}$ (Bolatto et al. 2013). And the velocity range of 46.0–50.3 km s^{-1} was selected to obtain the intensity of the CO line, W_{CO}, given in units of K km s^{-1}. The total mass of the molecular material is calculated with

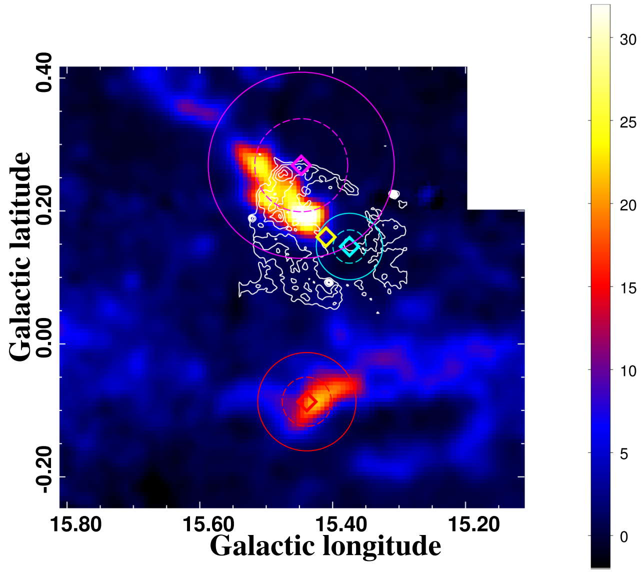

Figure 3. Integrated ^{13}CO($J = 1$-0) emission intensity (K km s^{-1}) toward SNR G15.4+0.1 in the velocity range of 46.0–50.3 km s^{-1}. The white contours show the radio emission at 3.3 GHz, as shown in Figure 1. The red and magenta diamonds show the positions of SrcA and SrcB1, which are spatially consistent with molecular clumps A and B, respectively. The cyan and yellow diamond mark the positions of SrcB2 and HESS J1818-154 (H. E. S. S. Collaboration et al. 2014), respectively. The dash and solid circles present the 1σ and 2σ error radii of SrcA, B1, and B2, respectively.

$$M = \mu m_H d^2 \Omega_{px} X_{CO} \sum_{px} W_{CO} \propto N_{H_2}, \qquad (1)$$

where μ is the mean molecular weight equal to 2.8, for which we assumed a relative helium abundance of 25% (Castelletti et al. 2013). m_H is the mass of the H nucleon, and Ω_{px} corresponds to the solid angle subtended for each pixel in the map. The term $\sum_{px}$ W_{CO} is obtained by summing the map content for the pixels in the desired sky region and in the desired velocity range. For clumps A and B, we estimated the total mass in a region of $0\overset{\circ}{.}1$ sky integration radius around the central position of SrcA and SrcB1, respectively. The total mass contents of clumps A and B are estimated to be about $2.4 \times 10^4 d_{4.8}^2 M_\odot$ and $3.3 \times 10^4 d_{4.8}^2 M_\odot$. Assuming a spherical geometry of the gas distribution, we

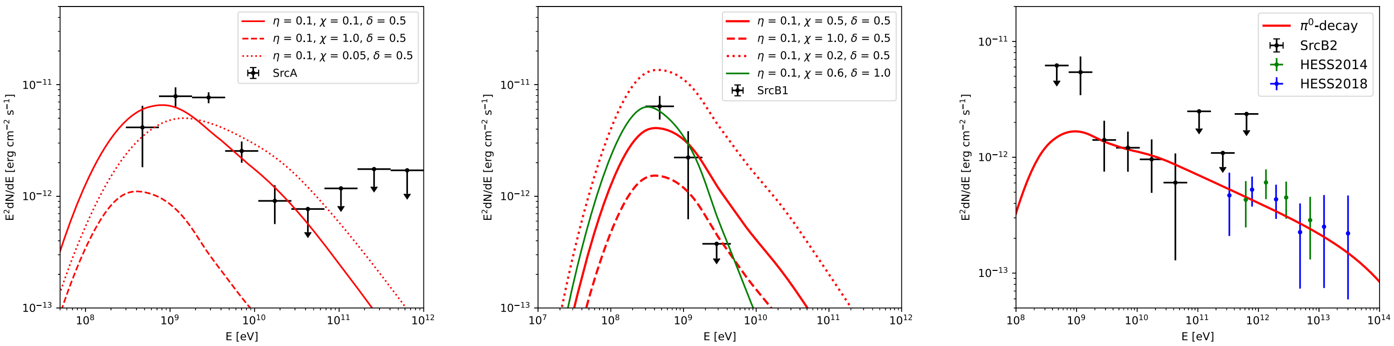

Figure 4. Modeling of the γ-ray spectra of SrcA (left), SrcB1 (middle), and SrcB2 (right) with the hadronic models. The solid, dashed, and dotted red lines for SrcA and SrcB1 indicate the scenarios with the different η, δ, and χ values shown in the legend. The solid red line for SrcB2 shows the hadronic model for a proton spectrum with an index of 2.3 and a cutoff energy of 3 PeV.

calcluated the corresponding average gas number densities to be about $n_{\rm A} = 400$ cm^{-3} and $n_{\rm B1} = 540$ cm^{-3}, respectively.

4. Discussion

The Fermi-LAT data analysis above shows that SrcB2 located at the center of SNR G15.4+1.0 is spatially coincident with HESS J1818-154, and its GeV spectrum also agrees with the TeV spectrum of HESS J1818-154. All this supports that SrcB2 is the counterpart of HESS J1818-154. And the global γ-ray spectrum of HESS J1818-154 can be described by a single power law with an index of ∼2.3. To determine the origin of the gamma-ray emission from HESS J1818-154, H. E. S. S. Collaboration et al. (2014) considered the PWN scenario powered by a hypothetical pulsar. However, the soft GeV γ-ray spectrum of HESS J1818-154 we detected means that it is much different from the typical γ-ray PWNe, such as HESS J1825-137 (Principe et al. 2020) and HESS J1640-465 (Xin et al. 2018; Mares et al. 2021). And the nondetection of the pulsar or diffuse emission in other wavelengths also disfavors the PWN scenario of the γ-ray emission from HESS J1818-154. The CO observation shows that SrcA is spatially consistent with molecular clump A, which is located outside the eastern border of the radio shell of SNR G15.4+1.0. And SrcB1, which is located at the edge of the radio shell of G15.4+1.0, is spatially well coincident with molecular clump B. The spatial coincidence between the γ-ray emission and the MoCs for SrcA and SrcB1 suggests that the γ-ray emission with the soft spectrum could be produced by the hadronic π^0 decay originating from the interaction between the clouds and CRs, which are accelerated in and escaped from SNR G15.4+0.1.

To explain the γ-ray emission from SrcA and SrcB1, we assume instantaneous injection of protons into a uniform emission zone A or zone B1 at $T = 8200$ yr ago. The spectrum of the injected protons is adopted to be a power law with an exponential cutoff,

$$Q(E) = Q_0 E^{-\Gamma} \exp\left(-\frac{E}{E_{\rm p,\,cut}}\right). \tag{2}$$

Here Γ and $E_{\rm p,\,cut}$ are the spectral index and the cutoff energy of protons, respectively. Considering the hard γ-ray spectrum of HESS J1818-154 and the spatial coincidence with SNR G15.4+0.1, HESS J1818-154 is suggested to be an injected source with $\Gamma = 2.3$. And the proton cutoff energy is assumed to be the energy of the CR knee with $E_{\rm p,\,cut} = 3$ PeV. Both the injected source and the emission zones are approximated to be point-like sources. The distance between them is $r_{\rm s}$. The differential density of the escaped proton distribution in the emission zone can then be derived as (Thoudam & Horandel 2012; Liu et al. 2020)

$$N_p(E,\,t) = \frac{Q(E)}{[4\pi D(E)T]^{\frac{3}{2}}} \exp\left(\frac{-r_{\rm s}^2}{4D(E)T}\right). \tag{3}$$

Here, the diffusion coefficient is set to be spatially constant in each emission zone and is taken to be $D(E) = \chi D_0 (E/E_0)^{\delta}$ for $E > E_0$, where $D_0 = 3 \times 10^{28}$ cm^2 s^{-1} at $E_0 = 10$ GeV, and $\delta = 1/2$ with Kraichnan turbulence (Ptuskin et al. 2006; Blasi 2013). And $\chi = 1$ corresponds to the typical value of the Galactic diffusion coefficient (Ptuskin et al. 2006; Blasi 2013). With the distance of 4.8 kpc, the physical distance between SrcA, SrcB1, and HESS J1818-154 is calculated to be $r_{\rm sA} = 21$ pc and $r_{\rm sB1} = 11$ pc, respectively. For an injected source spectrum given by $Q(E) \propto E^{-\Gamma}$ and $D(E) \propto E^{\delta}$, Equation (3) shows that the spectrum of escaped protons, $N_p(E)$, approximately equal to $Q(E)$ at low energies, where the diffusion radius defined as $r_{\rm diff} = \sqrt{4D(E)T}$ is much smaller than $r_{\rm s}$. And at high energies, $N_p(E)$ will follow $N_p(E) \propto E^{-\left(\Gamma + \frac{3}{2}\delta\right)}$, where the spectral break is shown at E$_b$ with $\sqrt{4D(E_b)T} = r_{\rm s}$.

In our model, the total energy of injected protons is assumed to be $W_{\rm inj} = \eta\, {\rm E_{SN}}$, where $E_{\rm SN}$ is the kinetic energy of the SNR with a typical value of 10^{51}erg. The fraction η of the kinetic energy converted into escaped proton energy and the correction factor χ of the diffusion coefficient are free parameters to produce the different spectra of escaped protons in the emission zones. The correspond γ-ray fluxes are calculated using the *naima* package (Zabalza 2015) with

$$\frac{dN_{\gamma}}{dE_{\gamma}} = \frac{n_{\rm gas} c}{4\pi d^2}\left(\frac{4}{3}\pi R_s^3\right) \int \frac{d\sigma_{pp}}{dE_{\gamma}} N_p(E,\,t) dE, \tag{4}$$

where the differential proton-proton inelastic cross section for γ-ray production, $d\sigma_{pp}/dE_{\gamma}$, is adopted from Kafexhiu et al. (2014). And the radius of the emission region, R_s, is calculated to be 8.4 pc with an angular radius of 0.1° and a distance of 4.8 kpc. The values of the ambient gas density, $n_{\rm gas}$, in the region of SrcA and SrcB1 are adopted to be $n_{\rm A} = 400$ cm^{-3} and $n_{\rm B1} = 540$ cm^{-3}, respectively.

For SrcA, the resulting hadronic γ-ray flux with the parameters $\eta = 0.1$ and $\chi = 0.1$ could explain the observational data, which are shown as the solid red line in the left panel of Figure 4. And the total energy of escaped protons above 1 GeV in this emission zone is calculated to be $W_{\rm p,A} = 1.26 \times 10^{48}$ erg. We note that the diffusion coefficient is one order of magnitude lower than the typical Galactic value. With a higher diffusion coefficient, e.g., $\chi = 1$, the total energy of the injected protons converted from kinetic energy should be much higher than 10^{50} erg ($\eta = 0.1$) to explain the γ-ray flux of SrcA, which is not reasonable. And the lower diffusion coefficient (e.g., $\chi = 0.05$) would result in a higher spectral break energy, which contradicts the soft γ-ray spectrum of SrcA at high energy. The parameters of $\eta = 0.1$ and $\chi = 0.5$ could marginally explain the γ-ray emission from SrcB1, and the total energy of protons above 1 GeV in this region is calculated to be $W_{\rm p,B1} = 9.5 \times 10^{47}$ erg. The soft γ-ray spectrum of SrcB1 and the upper limits for the low flux in the high-energy range imply a higher value for δ of the diffusion coefficient. An improved fitting result with $\chi = 0.6$ and $\delta = 1.0$ is shown as the solid green line in the middle panel of Figure 4. This soft spectrum could also imply that the γ-ray emission is dominated by the soft spectrum of protons that were recently accelerated by shocks in the MoC. To explain the γ-ray emission from SrcB2/HESS J1818-154, the proton distribution following the formula $Q(E)$ is adopted. And with a rough value of the ambient gas density in this region of $n_{\rm B2} = 40\,{\rm cm}^{-3}$ calculated based on the CO observation, the total energy of protons above 1 GeV is estimated to be about $W_{\rm p,B2} = 4.58 \times 10^{48}$ $({\rm n_{B2}}/40\ {\rm cm}^{-3})^{-1}$ erg.

5. Conclusion

We analyzed the GeV γ-ray emission in the vicinity of SNR G15.4+0.1 using 13 yr of Fermi-LAT data. And three γ-ray sources were detected, SrcA, SrcB1, and SrcB2. SrcA is located outside of the eastern border of the radio shell of SNR G15.4+0.1, and SrcB1 is located at the edge of the radio shell of the SNR. Two dense molecular clumps are shown in this region based on the CO observation, which are spatially consistent with the γ-ray emission from SrcA and SrcB1, respectively. SrcB2 is located at the center of SNR G15.4+0.1 and is spatially coincident with the TeV γ-ray source HESS J1818-154. And the respective γ-ray spectrum could smoothly connect, which supports the hypothesis that SrcB2 is the GeV counterpart of HESS J1818-154. The spatial coincidence of the γ-ray emission and the MoCs for SrcA and SrCB1 suggests that their γ-ray emission could originate from the hadronic π^0 decay due to the inelastic collisions between the clouds and CRs, which are accelerated in and escaped from SNR G15.4+0.1. With the assumption of a point-like instantaneous injection of protons, the γ-ray spectrum of SrcA can be explained by the model with a total energy of the injected protons of 10^{50} erg ($\eta = 0.1$), and the diffusion coefficient is lower than the typical Galactic value ($\chi = 0.1$). And the model with $\eta = 0.1$ and $\chi = 0.5$ could also marginally explain the γ-ray emission from SrcB1. The global γ-ray spectrum of SrcB2/HESS J1818-154 is consistent with the hadronic π^0 decay of a single power-law spectrum with an index of 2.3 for protons, which favors SNR G15.4+0.1 as the counterpart of HESS J1818-154.

We thank Haiming Zhang, Ruizhi Yang, and Xi Liu for invaluable discussions. This work makes use of molecular line data from the Boston University-FCRAO Galactic Ring Survey (GRS). This work is supported by the National Natural Science Foundation of China under the grants 12103040 and 12147208, the Natural Science Foundation for Young Scholars of Sichuan Province, China (No. 2022NSFSC1808), and the Fundamental Research Funds for the Central Universities (No. 2682022ZTPY013).

ORCID iDs

Yuliang Xin https://orcid.org/0000-0001-5135-5942
Siming Liu https://orcid.org/0000-0003-1039-9521
Yu He https://orcid.org/0000-0002-2745-9001

References

Abdo, A. A., Ackermann, M., Ajello, M., et al. 2009, ApJL, 706, L1
Abdo, A. A., Ackermann, M., Ajello, M., et al. 2010, ApJ, 712, 459
Abdollahi, S., Acero, F., Ackermann, M., et al. 2020, ApJS, 247, 33
Abdollahi, S., Acero, F., Baldini, L., et al. 2022, ApJS, 260, 53
Ackermann, M., Ajello, M., Allafort, A., et al. 2013, Sci, 339, 807
Aharonian, F., Akhperjanian, A. G., Bazer-Bachi, A. R., et al. 2008, A&A, 481, 401
Aharonian, F. A., Akhperjanian, A. G., Aye, K.-M., et al. 2004, Natur, 432, 75
Aharonian, F. A., & Atoyan, A. M. 1996, A&A, 309, 917
Akaike, H. 1974, ITAC, 19, 716
Atwood, W. B., Abdo, A. A., Ackermann, M., et al. 2009, ApJ, 697, 1071
Blasi, P. 2013, A&ARv, 21, 70
Bolatto, A. D., Wolfire, M., & Leroy, A. K. 2013, ARA&A, 51, 207
Brogan, C. L., Gelfand, J. D., Gaensler, B. M., Kassim, N. E., & Lazio, T. J. W. 2006, ApJL, 639, L25
Castelletti, G., Supan, L., Dubner, G., Joshi, B. C., & Surnis, M. P. 2013, A&A, 557, L15
Chevalier, R. A. 1974, ApJ, 188, 501
Frail, D. A., & Mitchell, G. F. 1998, ApJ, 508, 690
Gabici, S., Aharonian, F. A., & Casanova, S. 2009, MNRAS, 396, 1629
Giuliani, A., Cardillo, M., Tavani, M., et al. 2011, ApJL, 742, L30
Hanabata, Y., Katagiri, H., Hewitt, J. W., et al. 2014, ApJ, 786, 145
H. E. S. S. Collaboration, Abdalla, H., Abramowski, A., et al. 2018, A&A, 612, A1
H. E. S. S. Collaboration, Abramowski, A., Aharonian, F., et al. 2014, A&A, 562, A40
Helene, O. 1983, NIMPR, 212, 319
Hillas, A. M. 2005, JPhG, 31, R95
Jackson, J. M., Rathborne, J. M., Shah, R. Y., et al. 2006, ApJS, 163, 145
Jogler, T., & Funk, S. 2016, ApJ, 816, 100
Kafexhiu, E., Aharonian, F., Taylor, A. M., & Vila, G. S. 2014, PhRvD, 90, 123014
Kilpatrick, C. D., Bieging, J. H., & Rieke, G. H. 2016, ApJ, 816, 1
Lande, J., Ackermann, M., Allafort, A., et al. 2012, ApJ, 756, 5
Li, H., & Chen, Y. 2010, MNRAS, 409, L35
Liu, S., Zeng, H., Xin, Y., & Zhu, H. 2020, ApJL, 897, L34
MAGIC Collaboration, Acciari, V. A., Ansoldi, S., et al. 2023, A&A, 670, A8
Malkov, M. A., & Drury, L. O. 2001, RPPh, 64, 429
Mares, A., Lemoine-Goumard, M., Acero, F., et al. 2021, ApJ, 912, 158
Mattox, J. R., Bertsch, D. L., Chiang, J., et al. 1996, ApJ, 461, 396
Ohira, Y., Murase, K., & Yamazaki, R. 2011, MNRAS, 410, 1577
Peron, G., Aharonian, F., Casanova, S., Zanin, R., & Romoli, C. 2020, ApJL, 896, L23
Principe, G., Mitchell, A. M. W., Caroff, S., et al. 2020, A&A, 640, A76
Ptuskin, V. S., Moskalenko, I. V., Jones, F. C., Strong, A. W., & Zirakashvili, V. N. 2006, ApJ, 642, 902
Reach, W. T., Rho, J., & Jarrett, T. H. 2005, ApJ, 618, 297
Rodriguez Marrero, A. Y., Torres, D. F., de Cea del Pozo, E., Reimer, O., & Cillis, A. N. 2008, ApJ, 689, 213
Su, H.-Q., Zhang, M.-F., Zhu, H., & Wu, D. 2017, RAA, 17, 109
Supan, L., Castelletti, G., Joshi, B. C., Surnis, M. P., & Supanitsky, D. 2015, A&A, 576, A81
Thoudam, S., & Hörandel, J. R. 2012, MNRAS, 419, 624
Uchiyama, Y., Funk, S., Katagiri, H., et al. 2012, ApJL, 749, L35
Wood, M., Caputo, R., Charles, E., et al. 2017, ICRC (Busan), 301, 824
Xin, Y.-L., Liao, N.-H., Guo, X.-L., et al. 2018, ApJ, 867, 55
Zabalza, V. 2015, ICRC (The Hague), 34, 922